Computational and Structural Biotechnology Journal 20 (2022) 5729–5739

COMPUTATIONAL ANDSTRUCTURAL BIOTECHNOLOGY JOURNAL

journal homepage: www.elsevier.com/locate/csbj

Method article

Creating patient-specific vein models to characterize wall shear stress in hemodialysis population

Andrés Moya-Rodríguez [a,b,*], Bingqing Xie [b], Dylan Cook [b], Maren Klineberg [c], Sandeep Nathan [d], Mary Hammes [e,*], Anindita Basu [b,*]

[a] Biophysical Sciences Graduate Program, University of Chicago, Chicago, IL 60637, United States
[b] Section of Genetic Medicine, Department of Medicine, University of Chicago, Chicago, IL 60637, United States
[c] College, University of Chicago, Chicago, IL 60637, United States
[d] Section of Cardiology, Department of Medicine, University of Chicago, Chicago, IL 60637, United States
[e] Section of Nephrology, Department of Medicine, University of Chicago, Chicago, IL 60637, United States

ARTICLE INFO

Article history:
Received 28 July 2022
Received in revised form 4 October 2022
Accepted 4 October 2022
Available online 13 October 2022

ABSTRACT

End-Stage Renal Disease (ESRD) patients require arteriovenous fistulas (AVF) that allow a mature vein to withstand hemodialysis. Unfortunately, venous thrombosis and stenosis in the cephalic vein arch after AVF placement is common and heavily influenced by hemodynamics. To better assess forces and flow behavior in the cephalic arch, we have built patient-specific millifluidic models that allow us to explore the complex interplay between patient-specific vein geometry and fluctuating hemodynamics. These 3D models were created from patient-specific intravascular ultrasound and venogram images obtained three- and twelve-months post AVF creation and fabricated into soft elastomer-based millifluidic devices. Geometric validation of fabricated phantom millifluidic device shows successful replication of original computational 3D model. Millifluidic devices were perfused with a blood-mimicking fluid containing fluorescent tracer beads under steady-state physiologic cephalic vein flow conditions (20 mL/min). Particle image velocimetry was employed to calculate wall shear stress (WSS) across the cephalic arches. Experimental WSS profile evaluation reveals that the physiologic cephalic arch model yields WSS values within physiologic range [76–760 mPa]. Moreover, upon comparing WSS profiles across all models, it is noticeable that WSS values increase as vein diameter decreases, which further supports employed experimental and analysis strategy. The presented millifluidic devices show promise for experimental WSS characterization under pathologic flow conditions to contrast from calculated physiologic hemodynamics and better understand WSS influence on thrombosis and stenosis in hemodialysis patients.

1. Introduction

End-stage renal disease (ESRD) occurs when normal kidney function falls below 10–15 %, a time when renal replacement therapy becomes necessary to maintain life. The prevalence of ESRD in the US continues to rise, with >800,000 reported cases in 2019. Most of these patients (~85 %) receive regular hemodialysis [1,2]. Hemodialysis involves removing blood from the body and clearing in through an artificial kidney, which requires a vascular access. The best access with fewest complications is an arteriovenous fistula (AVF). Two thirds of all AVF in the US are placed in the upper arm using the brachiocephalic (BCF) configuration, which commonly fails due to cephalic arch stenosis (14–60 %) and thrombosis (17–28 %) [3–5]. This is in striking contrast to outcomes in other parts of the world, e.g., Japan, where the majority of AVFs are placed in the lower arm and have superior outcomes and longevity [3]. Differences have been attributed to lower flow AVF and superior cannulation techniques. Failed AVFs lead to missed hemodialysis sessions and contribute to the morbidity, mortality and financial burden of interventional procedures for patients with ESRD [6]. Our understanding of the mechanisms of access failure is incomplete because we lack specific tools to study these pathologies in AVF clinical scenarios. Traditional anti-platelet and anticoagulants do not effectively prevent or treat access thrombosis and can cause significant side effects [7,8]. In the absence of reliable clinical predictors of thrombosis, the current standard of care is to treat AVF thrombosis *a posteriori*. Consequently, there is an urgent need to define how thrombosis occurs in ESRD downstream from the vascular access in order to establish effective treatment options or preventative care.

* Corresponding authors.

https://doi.org/10.1016/j.csbj.2022.10.010

We concentrate on the cephalic arch as we posit that its geometric bend has rheological implications since this is where stenosis and thrombosis commonly occur [9,10]. Vascular pathogenesis that results in stenosis and thrombosis can be better understood if cephalic arch geometries and flow conditions are faithfully recreated for extensive *in vitro* studies. This way, hemodynamics can be dissected in terms of local acting forces which are intimately tied to vessel geometry, blood viscosity and flow rate. These forces are best described by wall shear stress (WSS). Previous studies have investigated the overall effects of WSS in different disease conditions and blood vessels in human [11–17] and animal models [18–20]. Some of these studies however, were limited by small number of patients [21] or used advanced imaging that is not available for standard patient care [22].

Although BCF creation initially increases overall WSS due to increased blood flow, vein remodeling causes low WSS to develop in the cephalic arch over time [9,23]. Several studies have explored the effects of WSS specifically in the context of the AVF [24,25] and suggest that oscillating flow conditions induce abnormal WSS that can contribute to intimal hyperplasia and resultant stenosis in the AVF [26]. We performed a five-year study of an ESRD patient cohort with upper arm BCF and observed that venous stenosis was common and that 40 % of patients experienced thrombosis that resulted in loss of access. We and others found that AVF placement predisposed the cephalic vein to increased blood flow velocity, pulsatile flow, areas of low WSS, and increased risk of stenosis and thrombosis [9,23,27–31].

Though computational models have shown the importance of the endothelium in thrombosis and been used to calculate WSS in the AVF, these models do not provide a research platform to perform perfusion experiments to test intervention options. Given the larger cephalic vein diameters and increased flow rates associated with AVF, microfluidic systems used to study arterial circulation are not applicable to study complex patient-specific hemodynamics in large vein geometries [32]. This paper highlights the development of a novel application of routine diagnostic measures, such as Intravascular Ultrasound (IVUS) and venogram, to create patient-specific millifluidic models of the cephalic vein arch downstream of flow in the AVF. We detail the fabrication of transparent elastomer-based millifluidic models *in vitro* that capture patient-specific dimensions, overall geometry and local topography of their venous cephalic arches. We validate our design and fabrication workflow on such an elastomeric device prototype. We then build fluidic devices that recreate the cephalic arches of two hemodialysis patients at two time points. The devices are perfused and imaged to characterize flow in each device, using an engineered fluid matching the viscosity and density of blood and containing tracer microbeads under steady-state physiological conditions. We also developed image analysis software to extract the velocity of the fluorescent tracer beads and calculate WSS from the imaged streamlines.

Although the current study details the interplay of geometry and hemodynamics under physiologic flow parameters, it is yet unable to implement pathologic flow rates or pulsatile waveforms, these models enable a comprehensive study of thrombosis under pathologic flow upon further optimization. The geometry and hemodynamics in the fluidic model matching the patient-specific abnormal flow conditions can help tease out the variability in thrombosis risk and outcome between patients. Our technology will allow systematic isolation and analysis of factors that play a critical role in the nucleation and propagation of thrombosis in an AVF, like vein geometry, flow parameters, blood constituents, and endothelial cell activation, to help develop personalized care in hemodialysis and improve the quality of life for ESRD patients.

2. Materials and methods

2.1. Device fabrication

Two time point-specific 3D models of the cephalic arches of two patients (P96 and P104) were reconstructed from IVUS and venogram of the cephalic arch taken 3 and 12 months (mo.) after AVF placement [29]. The physiologic and pathologic models were created in AutoCAD with an average diameter of 3 mm (physiologic) and 6 mm (pathologic) and bend angle of 125°. Importantly, the physiologic cephalic arch is much smaller than the (enlarged) pathological and patient-specific geometries presented in this study [33]. Significant and continuous dilation of the cephalic vein in patients accompany cephalic arch remodeling after AVF placement which is necessary to withstand high flow rates and pulsatile flow transmitted through the AVF from the bypass artery. These abnormal flow patterns transmitted into the cephalic arch through the AVF can perturb the steady-state, low-velocity flow seen under physiological conditions. We doubled the cephalic arch diameter to capture this vein dilation in the pathologic model.

Each model (Fig. 1A) was imported into AutoCAD and two cones, each 2 cm in height, were added to the two ends of each model to help stabilize the flow at the junctions between the vein model and the flow system (Fig. 1B). Additionally, a box-like mold was designed to ease fabrication of the millifluidic devices. The vein and box mold were exported as a.stl file and imported to Cura LulzBot Edition 3.2.21 software. 3D printing parameters were set to 0.38 mm resolution, printing temperature of 210 °C, with densities of 100 % and 10 % for the print and support, respectively. After adjusting the Print Setup, the file was exported as a GCode File (*.gcode) and transferred to the Taz4 3D printer (#LUKTPR0041NA, B&H Photo) using a water-soluble, polyvinyl alcohol filament (PVA; #PVA300N05, eSUN) for 3D printing (Fig. 1C).

Once the device and box mold were printed, the box mold was glued to a 150 mm × 15 mm polystyrene Petri dish (Sigma) with a hot glue gun. Polydimethylsiloxane (PDMS; Catalog # 4019862, Dow Sylgard 184) was mixed at 1:10 (cross-linker: base) ratio and poured on the inside of the box mold to form an initial thin layer. Air bubbles trapped within the PDMS mix were removed by placing the Petri dish in a vacuum desiccator for 30 min before curing at 65 °C for 2 hr. Subsequently, the 3D printed vein model was cleaned to remove all support filament and placed on top of the cured PDMS layer. Another PDMS layer was poured on the box and cured, covering half the height of the vein print. Upon vacuuming and curing, a final PDMS layer was poured and cured to completely cover the vein print. This resulted in a PDMS block with 3D printed vein embedded (Fig. 1D). The surrounding 3D printed box mold was removed by cutting out the PDMS block with a scalpel.

A 1 mm biopsy punch was used to cut into the PDMS to access the tips of the inlet and outlet cones. The device was immersed in DI water and autoclaved in a B4000-16 BioClave Research Autoclave (Benchmark Scientific) 4–5 times at 134 °C, 30 psi until the PVA printed models within the solidified PDMS block were dissolved (Fig. 1E). Once dissolved, a cavity that recapitulates the patient-specific vein geometry (as reconstructed by us from IVUS and venogram data) remained inside the PDMS device. The millifluidic device was submerged in boiling water and wiped rapidly to remove any PVA particulate adsorbed onto the device surface. Unless removed, the PVA particulate coating makes PDMS surfaces significantly cloudy, which can deteriorate quality of fluorescent images of the device obtained during flow experiments.

Since relatively high flow rates are necessary to mimic physiologic flow of the cephalic arch, it is critical that leakage-free connections between the fluid reservoirs and millifluidic devices are established. Given that our fluid reservoirs have tubing ports com-

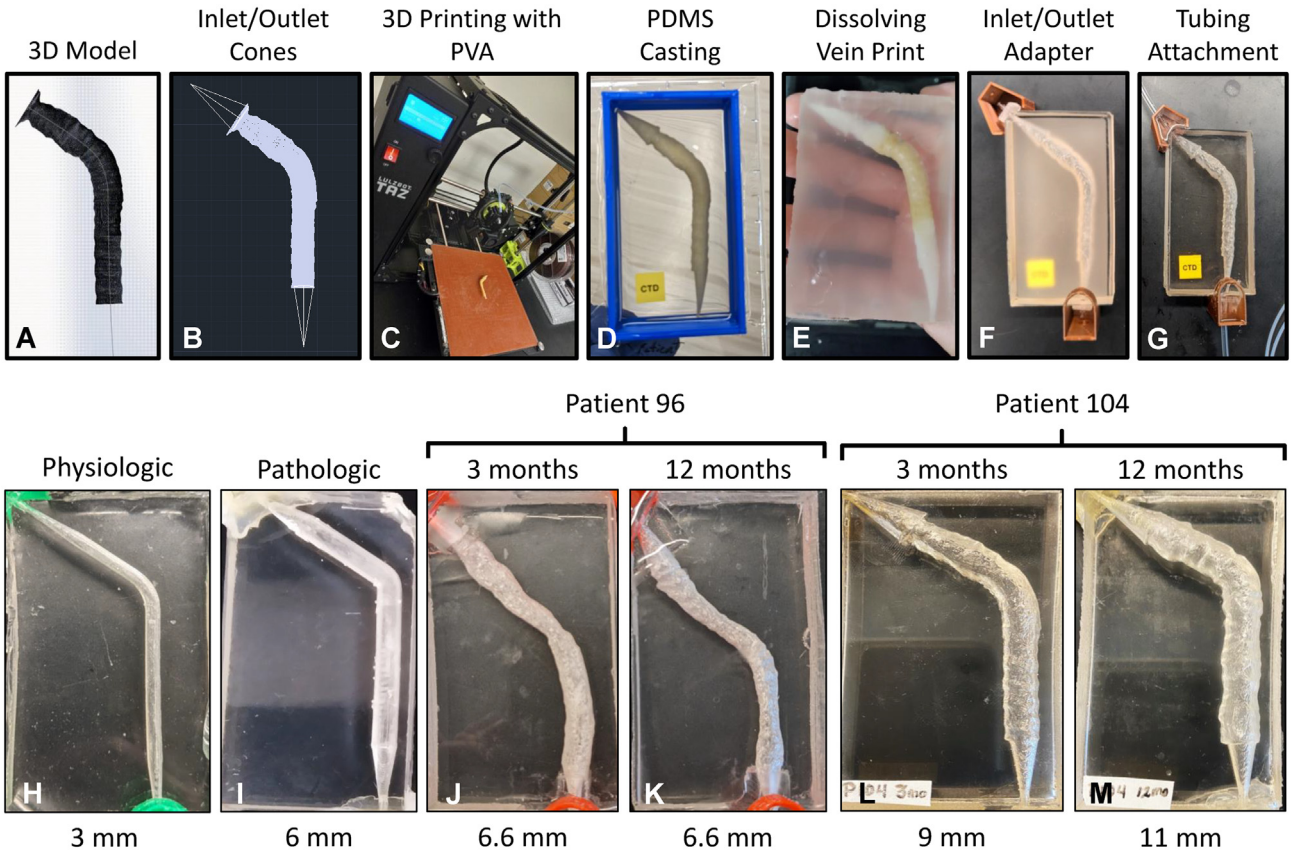

Fig. 1. Fabrication of cephalic arch millifluidic devices. (A) Patient computational cephalic arch model. (B) Inlet/outlet cones addition to computational model to make flow setup tubing compatible with fabricated millifluidic device inlet/outlet dimensions. (C) Computational model 3D printing with water-soluble PVA filament by material extrusion 3D printer. (D) Post-PDMS casting, the cephalic arch 3D print is encased in a PDMS block. (E) Inlet/outlet holes are made in the PDMS blocks and these are submerged in water and autoclaved until 3D print is completely dissolved. (F) Inlet/outlet adapters are incorporated to connect the millifluidic device to the flow setup and circuit. (G) Tubing is attached to connect it to fluid reservoirs in order to perform flow experiments and record them via epifluorescence microscopy. (H-M) Fabricated cephalic arch millifluidic devices and respective average vein diameters (mm) capturing physiologic (H), pathologic (I) and patient-specific geometries at 3 and 12 months post-AVF creation (J-M).

patible with 1/16″ outer diameter (OD), 1/32″ inner diameter (ID) PEEK tubing and our millifluidic devices have inlet/outlet ports compatible with 1/16″ ID, 1/8″ OD Tygon PVC clear tubing (#6516 T11, McMaster Carr), a cuffed tube-tube connection adapter was made to couple tubing. To achieve this, the ring portion of 8-gauge AWG crimp ring terminal connectors (#IGCRT8-10, Amazon) were cut with a sheet metal cutter (#DWHT14675, Amazon) in order to obtain a cast-able cylindrical mold. Around 4 cm of the PEEK tubing was inserted into the Tygon tubing. A rubber sleeve was positioned to tightly cover the PEEK tubing-Tygon tubing connection placed in the center of the mold. The bottom of the cylindrical mold was then sealed with Parafilm M wrapping film (#S37440, Fisher) to keep tubing components in place. The PEEK tubing-Tygon tubing junction was positioned vertically such that both tubing ends were coaxially aligned relative to the cylindrical mold. Low-viscosity epoxy resin (#4336899262, Amazon) was poured into the cylindrical mold to encase the tubing junction. The resin was allowed to cure at room temperature for at least 24 hr. to ensure that any potential leaks in the tubing junction were sealed (Fig. S1A).

To stabilize the junction between the millifluidic device and the coupled tubing adapter, two small 3D-printed box molds were used to cast PDMS (Fig. S1B). Plastic barbed tube fittings (3/32″ OD × 1/16″ ID, #5117 K41, McMaster-Carr) were plugged into both the inlet and outlet of all devices (Fig. 1F). The smaller box molds were aligned with the device inlet and outlet and affixed to the device using a hot glue gun. The Tygon-tubing end of the tubing adapter was connected to the barbed fitting at the device inlet through a hole in the small box mold; the outlet tubing was similarly attached to the barbed fitting on the device outlet. Finally, PDMS (1:10 crosslink/elastomer) was cast and cured on the small box molds to seal the junctions. The inlet tubing was connected to the fluid reservoir; the pressure-driven flow control system was also connected to the fluid reservoir to drive unidirectional flow in the millifluidic devices (Fig. 1G). The outlet tubing was allowed to drain out at atmospheric pressure. Six fluidic devices were fabricated: physiologic, pathologic, patient P96 imaged 3 (P96, 3 mo.) and 12 months (P96, 12 mo.) after AVF placement, and patient P104 also imaged 3 (P104, 3 mo.) and 12 months (P104, 12 mo.) after AVF placement. All fabricated devices are displayed in Fig. 1H-M, along with their average vein 'lumen' diameters.

Additionally, 'phantom' device, based on a patient (P98, 3 mo., average vein diameter = 8.5 mm) chosen at random, was created for geometric validation of our device fabrication method (Fig. 2A), to check if the internal cavity geometry of fabricated 'phantom' matched the geometry of the computational model it was based on. The inlet/outlet ports were simplified in the phantom model since flow was not necessary to image the internal cavity of this device.

2.2. Validating device fidelity in recapitulating cephalic arch geometry

To confirm that the internal vein geometry of our millifluidic devices matches the geometry of the computational models they

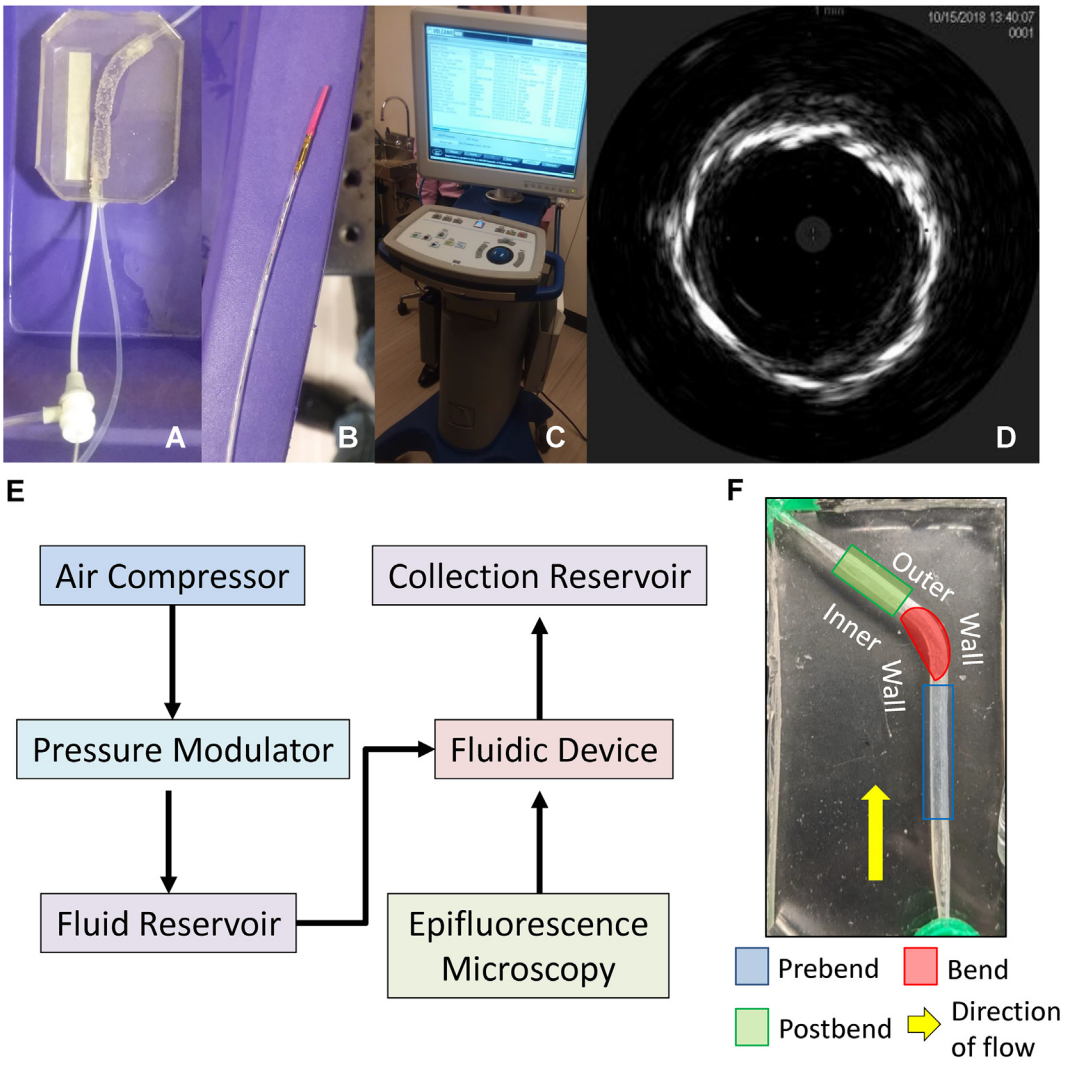

Fig. 2. Post-fabrication device geometric validation and flow imaging strategy. (A) Phantom model of the cephalic arch canulated with IVUS transducer catheter. (B) IVUS catheter. (C) Portable IVUS imaging console. (D) IVUS image obtained from the phantom model flushed with 1X PBS. (E) Component diagram of experimental flow/imaging setup. (F) Vein region diagram showing prebend (blue), bend (red) and postbend (green) and employed direction of flow (yellow arrow). (For interpretation of the references to color in this figure legend, the reader is referred to the web version of this article.)

are based on, we performed IVUS on the millifluidic phantom device, henceforth referred to as the 'phantom'. We generated 3D computational models constructed from each IVUS pullback imaging performed on the phantom device that could be used for geometric comparison. This process was followed to test consistency of IVUS imaging across different trials, as well as for fidelity of our 3D modeling and device fabrication processes in recapitulating vein geometry. We reasoned that if our phantom millifluidic model was faithful to the IVUS images, then the models reconstructed from different rounds of IVUS imaging of said device would match each other, as well as the original model used to fabricate the millifluidic device in the first place.

The millifluidic phantom device (Fig. 2A) was filled with 1X phosphate buffered saline (PBS), punctured using a 21G micro-puncture needle and a 0.018″ micro-puncture wire was inserted into the 'lumen' of the model, which served as a guide wire for the imaging catheter (Fig. 2B). Next, a 4 French (Fr) micro-puncture sheath was advanced over the guidewire and exchanged via a 0.035″ guidewire for a 5-Fr Cordis vascular introducer sheath (Cordis Corporation, Miami Lakes, FL), degassed, flushed and secured in place. Then, a Hi-Torque Floppy II coronary guidewire (Abbott Vascular, Santa Clara, CA) with 0.014″ x 190 cm dimensions was introduced into the lumen of the phantom and positioned distally. Finally, a Philips Volcano Eagle Eye Platinum 20 MHz Intravascular Ultrasound (IVUS) catheter was prepared, flushed and introduced over the coronary guidewire into the millifluidic phantom model and subsequently positioned within the proximal cephalic arch to simulate the *in vivo* starting IVUS position. The IVUS catheter was calibrated using the portable IVUS imaging console (Fig. 2C) to eliminate near-field ring-down artifact and the field of view was adjusted to ensure full circumferential visualization of the model (Fig. 2D). Interestingly, the contrast of the lumen images was higher in the PDMS millifluidic phantom model than in actual patient cephalic veins. Two independent IVUS pullback recordings in grayscale were performed using a research-quality pullback sled at a rate of 1.0 mm/s.

Venogram imaging was not required on the PDMS device; PDMS being transparent, allowed direct imaging of the general contour of the vein when perfused with food color dye. This image was processed using '*threshold*' and '*skeletonize*' functions in NIH ImageJ [34] to obtain the vein path. This was combined with the IVUS images of the millifluidic phantom device obtained as described above to reconstruct 3D models [29].

2.3. Flow setup

Millifluidic devices were imaged on an Olympus IX83 microscope (Fig. S1C), perfused with blood-mimicking fluid (BMF, distilled water with 6.3 % (w/v) Dextran, D4876-50G, Sigma-Aldrich) with viscosity = 3.5 mPa*s, density = 1.022 ± 0.001 g/mL and containing trace amounts ($4x10^{-6}$ %, v/v) of 2-μm fluorescent polystyrene microbeads (Catalog # FCDG008, Bangs Labs). A concentration of 4 % Dextran in BMF (w/v) with a viscosity = 2.4 mPa.s and density = 1.013 ± 0.001 g/mL was also used in some flow experiments. Comparing to physiologic blood, the reported viscosity range and density of human whole blood is [3.5–5] mPa*s and 0.994 ± 0.032 g/mL [35,36]. BMF was perfused into the millifluidic devices under physiologic steady-state flow at 20 mL/min [37], using an OB1 MK3 + pressure-driven flow control system (Elvesys, France; Fig. S1C). Component diagram of the fluidic circuit is shown (Fig. 2E).

2.4. Imaging

The steady-state flow at 20 mL/min represents a healthy flow rate for non-arterialized cephalic veins [37]. BMF was flowed at 20 mL/min into each device at steady-state to characterize WSS in the device as a function of local vein geometry; the flow rate was maintained while the cephalic arch models were imaged close to the device wall using epifluorescence microscopy. Image quality limitations only allowed imaging in areas close to the PDMS-BMF interface of the millifluidic device, henceforth referred to as the 'vein wall'. Focusing deeper into the BMF resulted in higher background fluorescence and also made the vein wall substantially more difficult to resolve in the images.

We imaged tracer beads flow close to the wall (≤400 μm) which was sufficient to calculate WSS across all Regions Of Interest (ROIs) in all models. Flow streamlines adjacent to the vein wall should accurately capture local flow velocities and WSS. Videos of flow trajectories of the fluorescent beads were imaged under 6.4X magnification (using a 4X, NA = 0.16 objective and 1.6X built-in microscope magnification) at 40 frames per second (fps) and 50–100 ms exposure times (depending on device), using a Hamamatsu ORCA Flash4.0 camera and MetaMorph software (Molecular Devices, USA) under GFP illumination (488 nm/510 nm). Videos consisting of 100 image frames, each frame containing 2048x2048 pixels, of tracer-bead streamlines were obtained from 18 to 22 positions, each referred to as an ROI, per device. At least 10 streamlines were extracted per image frame. This yielded fluorescent streaks of reasonable lengths from which local flow velocities were calculated across outer and inner walls of prebend, bend and postbend regions (Fig. 2F). Note that for a given flow velocity, longer exposure times lead to longer fluorescent streaks in the images (Fig. S1-D-F). Videos of 100 image frames each were acquired per ROI and saved as 16-bit.tiff files for subsequent data processing off-line. Overall, 18–22 ROIs were captured at a given flow rate per device, across prebend, bend and postbend regions.

2.5. Image processing

All videos needed to be pre-processed with a macro-code written in NIH ImageJ [34] to extract a) high-contrast streamlines, and b) outline of the vein wall for any given ROI, before using our automated Python-based pipeline to calculate flow velocity and WSS. ImageJ pre-processing (following functions performed sequentially on each raw image stack (Fig. 3A): contrast enhancement, background fluorescence subtraction, de-speckling, brightness and contrast adjustment (Fig. 3B), threshold adjustment (Fig. 3C), binarization, and 'Analyze Particles' to filter streamlines by size and circularity (Fig. 3D). The 'Analyze Particles' function is also useful to filter out image artifacts like diffraction rings, small debris, etc. Streamlines out of the focal plane that are less bright than the streamlines in the focal plane were filtered out. Given that experimental conditions such as flow rate, exposure time, magnification and numerical aperture of the objective, bead concentrations, etc. affected streamline quality and varied between experiments, the function parameters in the macro-code needed to be adjusted for each tiff-stack.

Identifying the vein wall boundary in the ROIs is important to calculate WSS. A maximum intensity Z-stack projection was made on the tiff-stack to generate a single wall boundary image from each ROI (Fig. 3E), manually outlined, binarized (Fig. 3F) and added to each frame of processed streamlines, using the '*Image Calculator*' function. These image pre-processing steps generated.tiff files of 100 frames each for each ROI, with each frame containing binarized streamlines of fluorescent beads and the vein wall outline (Fig. 3G).

Since the binarized images produced by the ImageJ preprocessing were less susceptible to variation, we developed a customized image processing pipeline in Python to calculate velocity and WSS from the pre-processed data from each ROI. Individual image frames ordered in time were generated in.tiff format for analysis. To extract velocity streamlines in each image frame, we used the '*connected components detection*' algorithm [38] in OpenCV, an open-source software package for computer vision [39], to obtain all connected objects in each image frame. Next, we assigned a tight rectangular bounding box to each connected component. Bounding boxes of those connected components that met the following criteria were selected as velocity streamlines per frame: size in pixels (area of the fitted bounding box ranging between [75, 9000]), shape (height/width ratio of the bounding box between [3, 100]), height in pixels between [15, 500], and width in pixels <50.

After assigning velocity streamlines to each frame, we aggregated all streamlines in an ROI (as time series.tiff) into a global frame. We reconstructed the vein wall boundary per frame from the binarized contour of the wall boundary marked in each frame. We projected the velocity streamlines perpendicularly onto the wall boundary. For each pixel in the wall boundary, we searched all streamlines in the frame and collected those streamlines that were projected at 90° onto the pixel point on the wall boundary (Fig. 3H). We also used the measured viscosity of the BMF and the perpendicular distance of detected streamlines to the wall boundary to calculate WSS. If multiple streamlines were projected to the same pixel in the wall boundary, an average WSS value was computed for the pixel.

Using the pipeline described above, we calculated frame-by-frame information on streamline count, mean velocity (mm/s) and mean WSS (mPa). Violin plots of the distribution of velocity (red) and WSS (green), calculated from the streamlines in each frame, are shown for a series of 100 frames acquired consecutively over time are shown for an ROI chosen at random (Fig. 3I), with blue dots indicating the mean values. For any given ROI, the velocity and WSS values fluctuate around an average that remains stable over time, as expected for constant flow rate. Violin plots for select ROIs on the prebend, bend and postbend regions (outer wall of the pathologic model) are shown in Fig. S2C.

2.6. Theory and calculations

Wall shear stress, τ was calculated as:

$$\tau = \eta \frac{v}{h}$$

where η is the fluid's dynamic viscosity, v is the streamline velocity and h is the distance between streamline and vein wall boundary.

Though the viscosity, η of blood and BMF are shear-thinning [40], we use an average value (3.5 mPa·s) for simplicity. This value was measured in BMF, using a rotational rheometer (Anton Paar

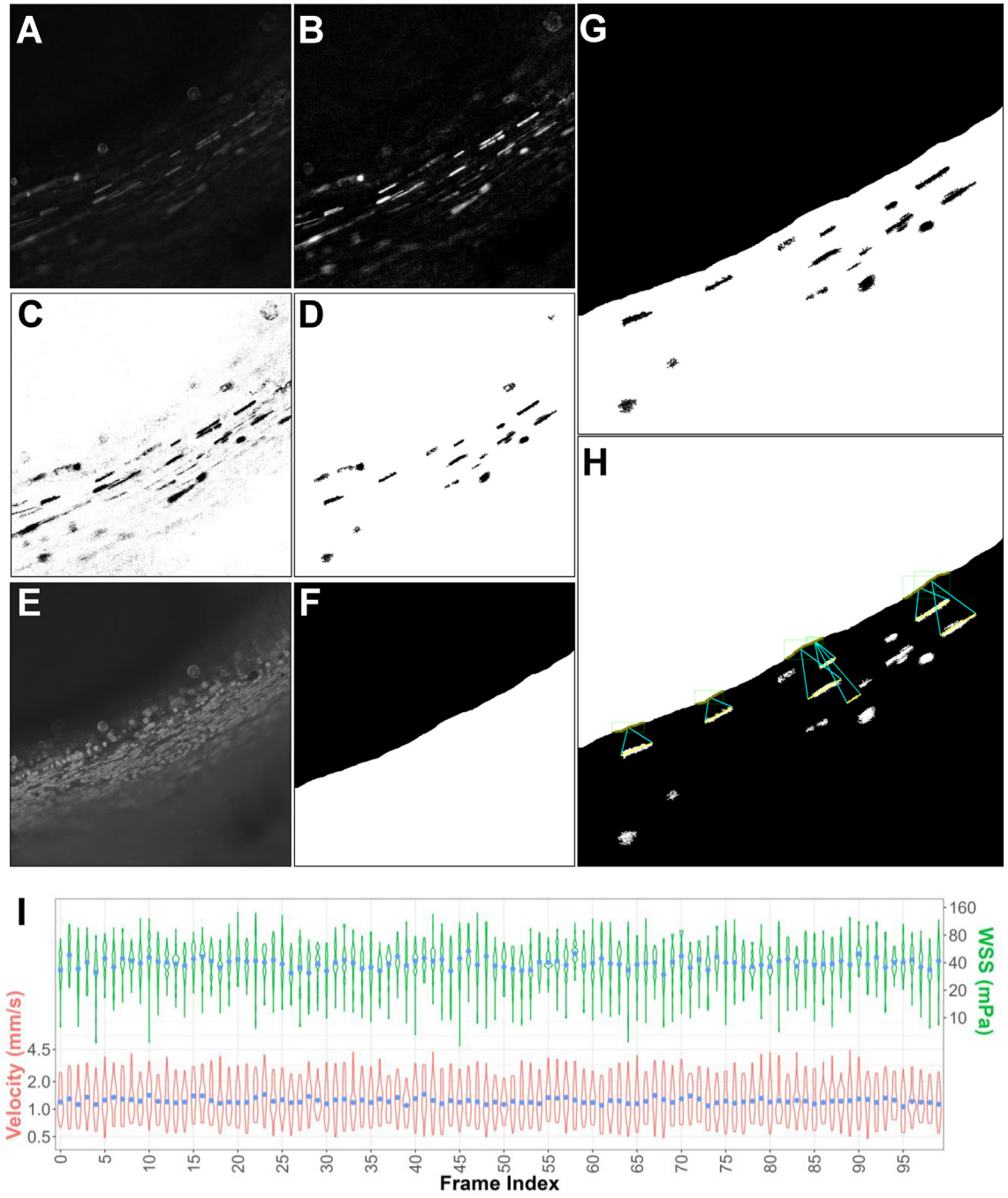

Fig. 3. Calculating streamline velocity and wall shear stress from particle imaging velocimetry. (A) ROI raw imaging data example from captured flow videos across the cephalic arch millifluidic devices. (B) Highlighted streamlines after sequentially: enhancing contrast, subtracting background, subtracting average intensity, despeckling and adjusting brightness and contrast (the latter being ROI dependent). (C) ROI dependent thresholding resulting in binary images that capture bright and well-defined streamlines. (D) Particle filtering by means of Analyze Particle function and adjusting size and circularity parameters to select for streamlines while filtering out low-quality out-of-focus streamlines and diffraction artifacts. (E) Max intensity projection of flow videos that facilitates outlining vein wall boundary. (F) Binary image generated after outlining vein wall boundary. (G) Addition of vein wall outline to filtered streamlines (D + F). (H) Streamline perpendicular projection onto vein wall boundary which allows calculating WSS. (I) Flow video analysis output for an outer wall postbend representative ROI from the pathologic model: WSS and streamline velocity violin plot across flow video frames. Blue dots represent the mean value for each frame.

MCR 301) under physiologic shear rates (20–200 s^{-1}) [41] The coefficient of variation (CV) for WSS is calculated as $CV(\%) = \left(\frac{standarddeviation_{WSS}}{mean_{WSS}}\right) * 100$. Given that a fixed flow rate was used in all experiments and vein diameter and surface topography influence flow velocity and WSS, we use CV to characterize and compare flow properties in geometrically diverse cephalic arch models used in this study.

3. Results

3.1. Validating phantom model

Two series of IVUS pullback measurements were performed on the phantom, referred to as 'OG', (Fig. 4A), each of which was used to generate a 3D model *in silico* (Fig. 4B, C), referred as 'Val1′ and

'Val2', respectively. 2D images of Val1 and Val2 in the xy-plane were captured at 5° rotational increment along the z-axis and coaxial to prebend vein path, up to 180° to compare the 3D models. Snapshots of OG, Val1 and Val2 were overlaid at each rotational angle and the overlap areas were calculated to quantify the differences in local topography. Fig. 4D shows the models (in black) at rotational angles of 0°, 45° and 90°, along with validation models area overlap relative to OG model (white).

The total area projection in xy-plane for OG, Val1 and Val2 across 180° rotational angles are shown in Fig. 4E, with an average overlap of 95.05 ± 3.92 % (Fig. 4F). This suggests that our 3D modeling of patient veins using IVUS and venogram imaging and 3D printing fabrication method yield reproducible vein models with relatively accurate representations of vein topographies. The Pearson correlation of the total areas between OG, Val1 and Val2 are > 0.5 across all rotational angles (Table 1). The area correlation between Val1 and Val2 is higher ($r_{(Val1\_Val2)}$ = 0.99) than either of these models with respect to OG ($r_{(OG\_Val1)}$ = 0.66 and $r_{(OG\_Val2)}$ = 0.62). We noted that IVUS imaging of the lumen in PDMS device offered higher contrast (Fig. 2D) compared to IVUS images of veins, potentially due to difference in material properties, leading to higher r value. Lower area correlation between the original and validation models could also result from the limited 3D-printing resolution. Overall, we see good agreement between the original and reconstructed models.

3.2. Hemodynamics under steady-state physiologic flow

ROIs in each device were grouped by the inner and outer walls of the prebend, bend and postbend regions and their WSS values were averaged to obtain a representative value for these regions. Average WSS values in the inner prebend, inner bend, inner postbend, outer prebend, outer bend and outer postbend regions in each device are shown in Fig. 5A. When averaging across all ROIs in a given model, we found that the highest average WSS value of 255 (±54) mPa was measured in the 'physiologic' device with the smallest average vein diameter (Table 2). Conversely, the lowest average WSS value, 27 (±6) mPa, was measured in the P104, 12 mo. device that also had the largest average vein diameter (Table 2). Overall, average WSS, calculated for all ROIs in a device, scaled inversely with the average vein diameter of the device, as expected (Fig. S3D).

WSS values measured in the physiologic model under physiological flow rates ranged between 203 ± 73 mPa in the inner bend to 346 ± 229 mPa in the outer prebend regions (Fig. 5A). Note that these values lie within the range of physiologic WSS values reported earlier [42].

Next, we compared WSS in the physiologic and pathologic models that have same arch angle but different vein diameters (3 and 6 mm, respectively). We measured relatively symmetric WSS in the bend region and striking asymmetry in the postbend region in the physiologic model (Fig. 5A, S3A). This agrees with fluid dynamics principles in pipe flow at geometric bends [29], where higher velocities are expected at the outer wall of the postbend region, along with lower velocities close to the opposite wall (inner bend). WSS polarization in the prebend region is absent in the pathologic model, consistent with shorter velocity streamlines measured in the pathologic model, at similar volumetric flow rates [29].

Focusing on the patient models, despite patient P96 having similar average diameters (6.6 mm) and arch angles (133° and 132° at 3- and 12-mo., respectively), we identified significant geometric

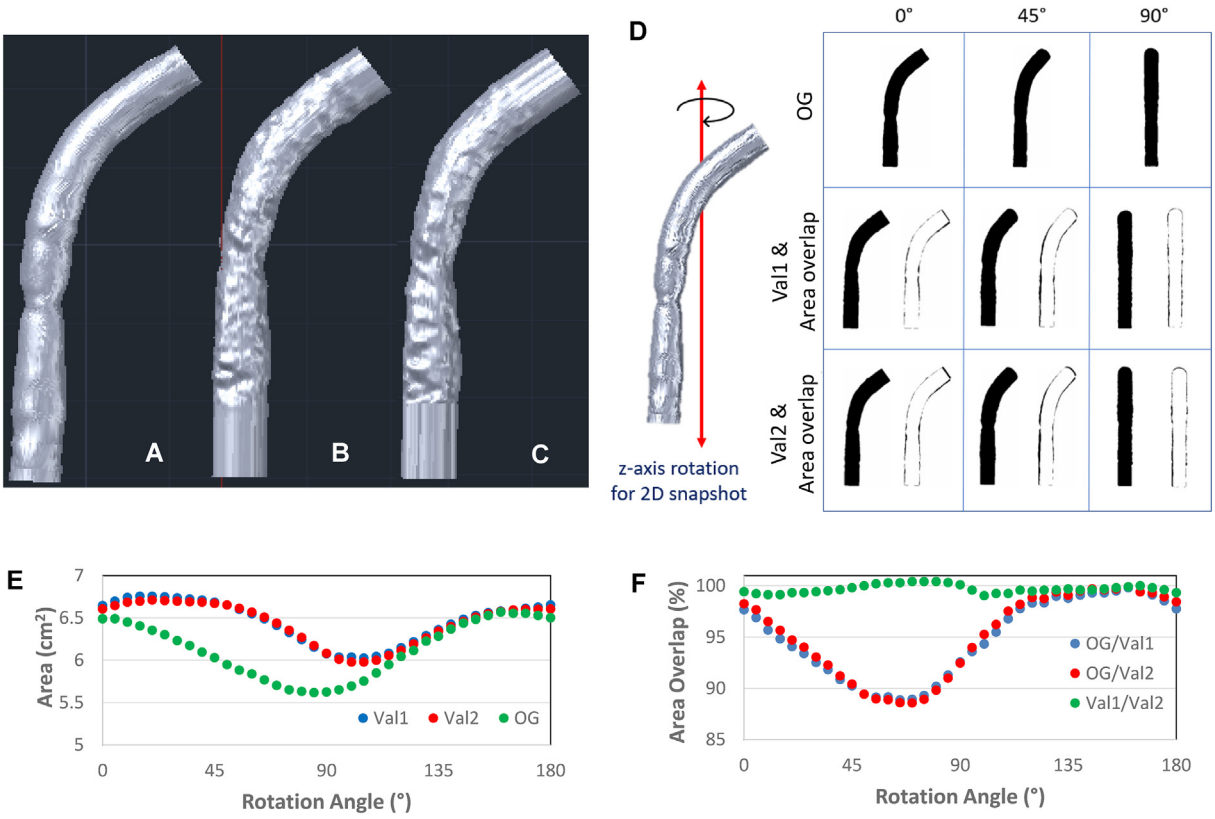

Fig. 4. Validation of the computationally reconstructed phantom model. (A) Original phantom computational model used for device fabrication. (B-C) Validation models reconstructed from IVUS and optical imaging performed on phantom millifluidic device (replicates). (D) Geometric validation strategy schematic: all models were rotated with respect to the z-axis and 2D images from top perspective were overlapped to evaluate area overlap from 0 to 180° rotational angles with 5° rotational increments. (E) Area values for all models across 180° of z-axis rotation. (F) Area overlap between phantom computational models upon z-axis rotation.

Table 1
Area comparative analysis of original and validation phantom computational models.

Phantom Model	Mean Total Area (cm^2)	Compared Models	Mean Area Overlap (%)	Area Pearson Coefficient (r)
Original	6.13 (±0.33)	$\frac{OG}{Val1}$	94.90 (±3.87)	0.66
Validation #1	6.46 (±0.25)	$\frac{OG}{Val2}$	95.20 (±4.08)	0.62
Validation #2	6.44 (±0.24)	$\frac{Val1}{Val2}$	99.70 (±0.40)	0.99

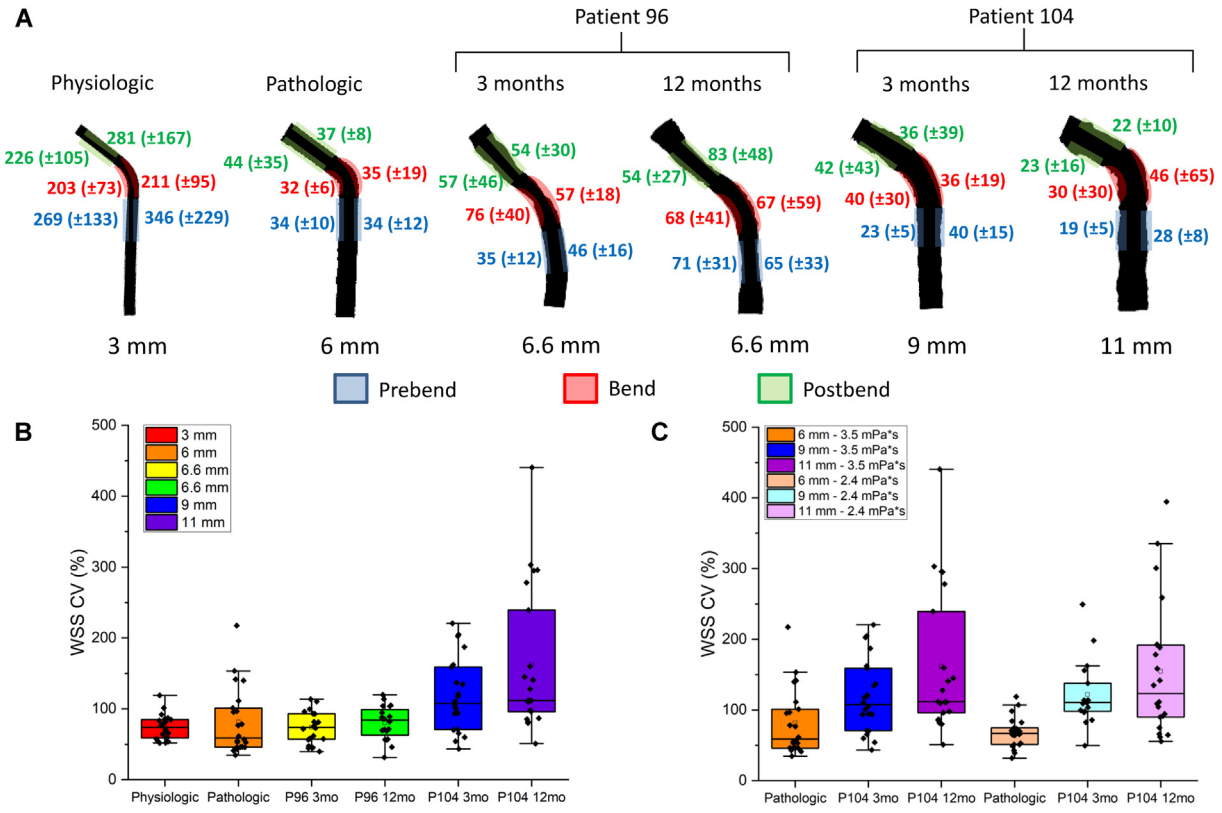

Fig. 5. WSS profiles across cephalic arch millifluidic models. (A) Experimental WSS profiles depicts the average WSS (mPa) value per vein region and wall side under normal physiologic flow of 20 mL/min using a blood-mimicking fluid. Vein model average vein diameter (mm) is shown below each cephalic arch outline. (B) WSS CV box plot across all models and their respective ROIs, average vein diameters shown on legend. Flow data was collected using BMF with viscosity of 3.5 mPa*s under physiologic flow. (C) WSS CV box plot for pathologic and P104 cephalic arch models under physiologic flow using BMF of varying viscosity (2.4 and 3.5 mPa*s). Average vein diameters and BMF viscosity are shown on legend.

Table 2
Geometric parameters, BMF viscosity, experimental WSS values (min, max, global average and median), mean frames per flow video, WSS CV values and ROI wall coverage values across cephalic arch millifluidic devices under physiologic flow.

Model	Diameter (mm)	Vein Surface Topography	BMF Viscosity (mPa*s)	Min WSS (mPa)	Max WSS (mPa)	Global Average WSS (mPa)	WSS Median (mPa)	Mean Frames per Flow Video	Average WSS CV (%)	Average ROI Wall Coverage (%)
Physiologic	3	Smooth	3.5	34.13	2688.16	255.38 (±54.08)	199.35	99.95	73.98	96.67
Pathologic	6	Smooth	3.5	4.56	479.55	34.52 (±1.36)	29.48	99.95	81.54	96.02
P96 3mo	6.6	Rough	3.5	8.29	431.44	54.11 (±10.32)	43.34	100.00	73.92	89.12
P96 12mo	6.6	Rough	3.5	11.92	561.90	70.76 (±3.26)	53.70	100.00	79.99	88.25
P104 3mo	9	Rough	3.5	3.23	1261.63	35.75 (±3.91)	22.04	99.55	118.61	97.92
P104 12mo	11	Rough	3.5	3.58	1132.31	26.89 (±6.18)	15.94	99.73	161.87	97.15

remodeling of the cephalic arch in 3D, particularly at the postbend region, which narrowed between 3 and 12 mo. (Fig. S3B). These geometric changes influence resulting WSS across different regions of the cephalic arch. For example, we observed increase in WSS in the prebend region and the outer wall of the postbend region from 3 to 12 mo. Moreover, WSS evens out in the bend region at 12-months, which contrasts the striking asymmetry observed at 3 mo. These findings indicate that vein dilation and remodeling can prominently affect hemodynamics in the cephalic arch through geometric and topographical changes.

Using the pathologic and P96 models to compare veins of similar sizes (6 and 6.6 mm, respectively), we note differences in WSS patterns in the prebend and bend regions between the models. Except for the postbend region, the pathologic model has similar WSS magnitudes on the inner and outer walls. This is not the case for P96 models at 3 and 12 mo. where WSS is asymmetric in the inner and outer bend, across all regions. This is most likely due to the uneven topography of the vein walls in P96, compared to the smooth wall of pathologic model and symmetric geometry along the vein lumen (Fig. 5A, S3A-B). For patient P104, the average vein diameter increases from 9 mm to 11 mm and arch angle decreases from 125° to 115° between 3 and 12 mo., respectively (Fig. 5A, S3C). Except for the outer bend region in P104, there is consistent decrease in WSS at decreased flow velocity due to increase in vein diameter (at fixed volumetric flow rate).

Since we are also interested in gauging variability in patient outcome, we quantified the WSS CV across the geometrically distinct models in context of vein diameter and topography. At fixed volumetric flow rate, we measure greater CV in average WSS with increased vein diameter (Fig. 5B). Devices with narrower veins, e.g., physiologic device (3 mm), show lower average WSS CV (74 %), whereas devices with larger vein diameter (11 mm in P104, 12 mo.) record larger CV (162 %, Table 2). We also characterized WSS and CV in the pathologic and P104 (3 and 12 mo.) devices at 20 mL/min at two different viscosities, 2.4 and 3.5 mPa·s (Fig. S3E, 5C), by adjusting the concentration of dextran in BMF (4 and 6.3 %, w/v, respectively). We found reproducible trends at these viscosities, where WSS CV increased systematically with average vein diameter: the pathologic model (6 mm) showed the lowest CV, followed by the CV in P104, 3 mo. (9 mm) and P104, 12 mo. (11 mm) models (Fig. 5C). We noted lower average WSS and standard deviation at 2.4 mPa·s, compared to 3.5 mPa·s (Fig. S3E). These results highlight the complexity of the system where vein diameter, geometry, surface topography and viscosity contribute to WSS in the cephalic arch.

4. Discussion

Previous studies reported a wide range of WSS values in different blood vessels that were associated with stenosis and thrombosis. Experiments on porcine models found that carotid artery stenosis was correlated with lower WSS (~800 mPa), compared to non-stenosed artery (WSS ~4070 mPa) [18]. In patients with moderately stenosed carotid arteries, Zhang et al. found that average axial WSS in local high and low-risk plaques was of 200 and 150 mPa, respectively [11]. AVF regions prone to neointimal hyperplasia (in a canine model for AVF stenosis) experienced a WSS range of [340–17,300] mPa while non-stenosed regions experienced a range of [1150–11,730] mPa [19] which makes it difficult to determine pathologic WSS given the range overlap. Studies in saphenous vein grafts and pulmonary veins report stenosis-inducing WSS levels at 1200 mPa and >1000 mPa, respectively [12,21]. WSS >40,000 mPa can cause endothelial denudation [30].

Collectively, non-pathologic and pathologic WSS in different vascular systems (venous and arterial) and model organisms reported in literature often overlap, making it difficult to truly understand WSS influence in AVF maturation and patency [20]. Colley et al. suggest that there is an optimal WSS range for specific vascular segments and result in vascular pathologies upon surpassing the range in either direction [43]. Given the inherent variation in native blood vessel geometries and physiologic flow rates, what may be considered as pathologic WSS (i.e., inducing stenosis and/or thrombosis), has to be evaluated for a specific vein or artery using patient-specific parameters. Overall, patient-specific geometries and hemodynamic conditions are necessary to understand how WSS affect stenosis and thrombosis risk in each patient through the course of hemodialysis.

In the current study, we present the design and operation of a novel patient-specific model of the venous cephalic arch to accurately measure WSS. We validated the fidelity in recreating patient vein geometry in the model, using IVUS imaging and infused these models with engineered fluids that mimic blood density and viscosity under physiologic flow conditions on the devices. We imaged the details of the particles flowing through our model vessel and constructed a semi-automated image analysis pipeline to determine WSS. WSS is an important measurement as the magnitude of the WSS in a cephalic vein is a predictor of vein remodeling in AVF. Currently, it is not possible to measure WSS accurately in clinical practice and past computational models defining WSS are limited in imaging and validation [24]. The clinical relevance of this tool, however, is yet to be determined.

This study presents the fabrication of fluidic models that recreate patient-specific vein geometry using radiologic and ultrasound imaging. It is evident from the patient models (e.g., P96 and P104 at 3 and 12 mo.) that cephalic arches of different patients responded differently in terms of vein remodeling to AVF placement and hemodialysis. We saw that average WSS decreased with increase in average vein diameter (Fig. S3D); however, patient-specific vein geometry and wall topography also influenced WSS. CV in average WSS, however, roughly increased with increase in vein diameter (Fig. 5B). Surface topography does not seem to be a major contributor to WSS CV under physiologic flow condition. For example, comparing the pathologic and P96 models with roughly similar vein diameters but marked different geometry and wall topography, the pathologic model recorded lower WSS than the P96 models but all three models showed similar CV.

We found that the physiologic model and P96 models, the latter being more than double the diameter of the former and topographically rugged, had very similar CV values. Thus, surface topography does not seem to be a major contributor to WSS dispersion in relation to mean WSS in relatively small veins under physiologic flow. Moreover, comparable CV values are also obtained within the pathologic model, where the vein is twice times as wide as the physiologic model. Nonetheless, topographical descriptions of these models are strictly qualitative, so devising a quantifiable measure of ruggedness will progress our understanding of topography-WSS interplay.

Blood viscosity, a crucial factor influencing WSS, can fluctuate over time in a patient-specific manner [44]. We identified significant effect of viscosity on WSS (Fig. S3E) but not on its CV (Fig. 5C). Changes in whole blood viscosity and WSS likely trigger endothelial cell activation before and after hemodialysis sessions where solute concentrations and osmotic pressures are readjusted, especially when treatment is administered three times a week [45].

Limitations and future directions: An eddy in the prebend region (Fig. S4A), generated by a mismatch in tubing and device diameters, prevented us from imaging steady-state laminar flow throughout the device. In future studies, we will mitigate the effect by replacing our current connection tubing of 1/32″ ID with wider tubing. This will create a more gradual transition in flow velocities from tubing to vein model, thus decreasing the size of the eddy. Preliminary experiments with wider tubing seem to eliminate any eddy formation in the prebend region (Fig. S4B), though further experiments are needed to confirm if this holds true across all models and different experimental conditions. We also expect that larger ID connection tubing will allow us to achieve (higher) pathologic flow rates. Note that the size and magnitude of this eddy in the prebend also depend on viscosity, a parameter that varies from patient to patient.

Currently, our models reliably achieve flow rates of 20 mL/min seen in physiologic conditions but falls far short of flow rates

>600 mL/min seen in patients under hemodialysis [32]. Additionally, we are developing the capability to modulate flow rates in a programmable way on our current setup to match patient-specific pulse profiles, along with data processing tools to calculate WSS under pulsatile flow [28]. These flow parameters are also of interest since pulsed flow in veins, coupled with dramatically increased flow rates might synergize together, resulting in thrombosis and clotting pathology in the hemodialysis population.

Due to limitations in imaging setup (objective with low NA (0.16), imaging through thick layers of PDMS and high scattering), we were unable to image deep into the fluidic devices. As a consequence, we limit WSS measurements to the lower half of the vein (closer to the objective). However, the asymmetric geometry of the fluidic models requires better coverage in imaging the devices in the current configuration, including their upper half. This and overall better resolution in z axis can be achieved by using confocal microscopy, objective with high NA and long working distance, and lower concentration of tracer beads in flow experiments. Additionally, newer 3D printer models are now capable of XY and Z-layer printing resolutions that surpass TAZ4 3D printer used in this study. It is reasonable to expect higher correlations and area overlap between original phantom and validation models by using 3D printers with higher spatial resolution.

Finally, adding a layer of endothelial cells to the inner walls of these millifluidic devices [46] and quantifying their biochemical responses under flow [47–49] are necessary to biologically complement generated WSS profiles [29].

Nonetheless, the present work shows that we have developed a robust workflow and image analysis pipeline to characterize WSS under healthy, physiologic flow conditions, a base knowledge needed to contrast from pathologic findings in the future. Also, if venous blood clots can be recreated *in vitro* in our devices, extracted and studied by histological and biochemical methods, they can lead to the synthesis of novel and more efficient anticoagulant and thrombolytic therapies that help decrease lethal thrombotic events.

5. Conclusions

In this work, we explored diverse geometries of the cephalic arch in hemodialysis patients with AVF. Nonetheless, we must recognize that vein physiology is constantly evolving and adapting to genetic and environmental inputs, especially in artificial circulatory scenarios such as AVFs. Therefore, in order to address current AVF failure rate, we set out to design and fabricate patient-specific cephalic arch replicas in the form of millifluidic devices to characterize hemodynamics and WSS under physiologic flow. We also created an image analysis pipeline to characterize flow and calculate WSS from videos of tracer particle streamlines. We applied novel 3D printing and advanced biomedical imaging technologies to study fistulas and connected vessels that are affected by thrombosis. To our knowledge, this is the first experimental work to generate patient-specific AVF vein models to help characterize geometric and flow abnormalities that underlie thrombosis and associated pathologies in the clinical setting.

CRediT authorship contribution statement

Andrés Moya-Rodríguez: Conceptualization, Writing – original draft, Funding acquisition, Project administration, Methodology, Validation, Software, Data curation, Formal analysis, Visualization, Investigation, Writing – review & editing. **Bingqing Xie:** Software, Data curation, Formal analysis, Visualization, Writing – review & editing. **Dylan Cook:** Methodology, Validation, Investigation, Writing - review & editing. **Maren Klineberg:** Methodology, Validation, Investigation. **Sandeep Nathan:** Methodology, Validation. **Mary Hammes:** Conceptualization, Writing – original draft, Funding acquisition, Project administration, Resources, Supervision, Writing – review & editing. **Anindita Basu:** Conceptualization, Writing – original draft, Funding acquisition, Project administration, Resources, Supervision, Writing – review & editing.

Declaration of Competing Interest

The authors declare that they have no known competing financial interests or personal relationships that could have appeared to influence the work reported in this paper.

Acknowledgements

We thank Supratik Guha and Abhiteja Konda for fabrication help and all patients who gave their time for imaging procedures. This work made use of the shared facilities at the University of Chicago Materials Research Science and Engineering Center, supported by National Science Foundation under award number DMR-2011854.

Funding

This work was supported by the Ginny and Simon Aronson Research Award, University of Chicago Institute of Translational Medicine Pilot Award, and A.B.'s research development funds. A. M−R. was supported by the NSF GRFP fellowship.

Appendix A. Supplementary data

Supplementary data to this article can be found online at https://doi.org/10.1016/j.csbj.2022.10.010.

References

[1] System USRD. 2021 USRDS Annual Data Report: Epidemiology of kidney disease in the United States. National Institutes of Health, National Institute of Diabetes and Digestive and Kidney Diseases, Bethesda, MD:, 202Report No.
[2] Bello AK, Okpechi IG, Osman MA, Cho Y, Htay H, Jha V, et al. Epidemiology of haemodialysis outcomes. Nat Rev Nephrol 2022;18(6):378–95. https://doi.org/10.1038/s41581-022-00542-7.
[3] Pisoni RL, Zepel L, Fluck R, Lok CE, Kawanishi H, Süleymanlar G, et al. International differences in the location and use of arteriovenous accesses created for hemodialysis: results from the dialysis outcomes and practice patterns study (DOPPS). Am J Kidney Dis 2018;71(4):469–78. https://doi.org/10.1053/j.ajkd.2017.09.012.
[4] Casserly LF, Dember LM. Thrombosis in end-stage renal disease. Semin Dial 2003;16(3):245–56. https://doi.org/10.1046/j.1525-139X.2003.16048.x.
[5] Quencer KB, Oklu R. Hemodialysis access thrombosis. Cardiovasc Diagn Ther. 2017;7(Suppl 3):S299-S308. 10.21037/cdt.2017.09.08. PubMed PMID: 29399534.
[6] Thamer M, Lee TC, Wasse H, Glickman MH, Qian J, Gottlieb D, et al. Medicare costs associated with arteriovenous fistulas among US hemodialysis patients. Am J Kidney Dis 2018;72(1):10–8. https://doi.org/10.1053/j.ajkd.2018.01.034.
[7] Kaufman JS. Antithrombotic Agents and the Prevention of Access Thrombosis. 2000;13(1):40-6. 10.1046/j.1525-139x.2000.00012.x.
[8] Dember LM, Beck GJ, Allon M, Delmez JA, Dixon BS, Greenberg A, et al. Effect of clopidogrel on early failure of arteriovenous fistulas for hemodialysis: A randomized controlled trial. JAMA 2008;299(18):2164–71. https://doi.org/10.1001/jama.299.18.2164 %J JAMA.
[9] Hammes M, Boghosian M, Cassel K, Watson S, Funaki B, Doshi T, et al. Increased inlet blood flow velocity predicts low wall shear stress in the cephalic arch of patients with brachiocephalic fistula access. PLoS ONE 2016;11(4). https://doi.org/10.1371/journal.pone.0152873.
[10] Kim Y, Kim HD, Chung BH, Park CW, Yang CW, Kim Y-S. Clinical predictors of recurrent cephalic arch stenosis and impact of the access flow reduction on the patency rate. J Vasc Access 2021;23(5):718–24. https://doi.org/10.1177/1129729821100875 8.
[11] Zhang G, Zhang S, Qin Y, Fang J, Tang X, Li L, et al. Differences in wall shear stress between high-risk and low-risk plaques in patients with moderate carotid artery stenosis: A 4D flow MRI study. Front Neurosci 2021;15.
[12] Khan MO, Tran JS, Zhu H, Boyd J, Packard RRS, Karlsberg RP, et al. low wall shear stress is associated with saphenous vein graft stenosis in patients with coronary artery bypass grafting. J Cardiovasc Transl Res 2021;14(4):770–81. https://doi.org/10.1007/s12265-020-09982-7.

[13] Vachharajani TJ, Taliercio JJ, Anvari E. New devices and technologies for hemodialysis vascular access: A review. Am J Kidney Dis 2021;78(1):116–24. https://doi.org/10.1053/j.ajkd.2020.11.027.
[14] Huang EP-Y, Li M-F, Hsiao C-C, Chen H-Y, Wu P-A, Liang H-L. Undersized stent graft for treatment of cephalic arch stenosis in arteriovenous hemodialysis access. Scientific Reports. 2020;10(1):12501. 10.1038/s41598-020-69402-3.
[15] Bai H, Sadaghianloo N, Gorecka J, Liu S, Ono S, Ramachandra AB, et al. Artery to vein configuration of arteriovenous fistula improves hemodynamics to increase maturation and patency. Science Translational Medicine. 2020;12 (557):eaax7613. 10.1126/scitranslmed.aax7613.
[16] Iwai R, Shimazaki T, Kawakubo Y, Fukami K, Ata S, Yokoyama T, et al. Quantification and visualization of reliable hemodynamics evaluation based on non-contact arteriovenous fistula measurement. Sensors [Internet] 2022;22(7).
[17] Bozzetto M, Soliveri L, Poloni S, Brambilla P, Curtò D, Condemi GC, et al. Arteriovenous fistula creation with VasQTM device: A feasibility study to reveal hemodynamic implications. The Journal of Vascular Access. 2022:11297298221087160. 10.1177/11297298221087160.
[18] Millon A, Sigovan M, Boussel L, Mathevet J-L, Louzier V, Paquet C, et al. Low WSS induces intimal thickening, while large WSS variation and inflammation induce medial thinning, in an animal model of atherosclerosis. PLoS ONE 2015;10(11):e0141880.
[19] Jia L, Wang L, Wei F, Yu H, Dong H, Wang B, et al. Effects of wall shear stress in venous neointimal hyperplasia of arteriovenous fistulae. Nephrology 2015;20 (5):335–42. https://doi.org/10.1111/nep.12394.
[20] Kudze T, Ono S, Fereydooni A, Gonzalez L, Isaji T, Hu H, et al. Altered hemodynamics during arteriovenous fistula remodeling leads to reduced fistula patency in female mice. JVS-Vasc Sci 2020;1:42–56. https://doi.org/10.1016/j.jvssci.2020.03.001.
[21] Hammer PE, McEnaney K, Callahan R, Baird CW, Hoganson DM, Jenkins KJ. The role of elevated wall shear stress in progression of pulmonary vein stenosis: evidence from two case studies. Children [Internet] 2021;8(9).
[22] Gunasekera S, Ng O, Thomas S, Varcoe R, de Silva C, Barber T. Tomographic PIV analysis of physiological flow conditions in a patient-specific arteriovenous fistula. Exp Fluids 2020;61(12):253. https://doi.org/10.1007/s00348-020-03085-4.
[23] Hammes M, Cassel K, Boghosian M, Watson S, Funaki B, Coe F. A cohort study showing correspondence of low wall shear stress and cephalic arch stenosis in brachiocephalic arteriovenous fistula access. J Vasc Access 2020;22(3):380–7. https://doi.org/10.1177/1129729820942048.
[24] Browne LD, Bashar K, Griffin P, Kavanagh EG, Walsh SR, Walsh MT. The role of shear stress in arteriovenous fistula maturation and failure: A systematic review. PLoS ONE 2016;10(12):e0145795.
[25] Remuzzi A, Bozzetto M, Brambilla P. Is shear stress the key factor for AVF maturation? J Vasc Access 2017;18(1_suppl):S10-S4. 10.5301/jva.5000686.
[26] Franzoni M, Cattaneo I, Longaretti L, Figliuzzi M, Ene-Iordache B, Remuzzi A. Endothelial cell activation by hemodynamic shear stress derived from arteriovenous fistula for hemodialysis access. Am J Physiol-Heart Circ Physiol 2015;310(1):H49–59. https://doi.org/10.1152/ajpheart.00098.2015.
[27] Sigovan M, Rayz V, Gasper W, Alley HF, Owens CD, Saloner D. Vascular remodeling in autogenous arterio-venous fistulas by MRI and CFD. Ann Biomed Eng 2013;41(4):657–68. https://doi.org/10.1007/s10439-012-0703-4.
[28] Ene-Iordache B, Remuzzi A. Disturbed flow in radial-cephalic arteriovenous fistulae for haemodialysis: Low and oscillating shear stress locates the sites of stenosis. Nephrol Dial Transplant 2012;27(1):358–68. https://doi.org/10.1093/ndt/gfr342.
[29] Hammes M, Moya-Rodriguez A, Bernstein C, Nathan S, Navuluri R, Basu A. Computational modeling of the cephalic arch predicts hemodynamic profiles in patients with brachiocephalic fistula access receiving hemodialysis. PLoS One 2021;16(7 July). 10.1371/journal.pone.0254016.
[30] Boghosian M, Cassel K, Hammes M, Funaki B, Kim S, Qian X, et al. Hemodynamics in the cephalic arch of a brachiocephalic fistula. Med Eng Phys 2014;36(7):822–30. https://doi.org/10.1016/j.medengphy.2014.03.001.
[31] Hammes M. Importance of the endothelium in arteriovenous fistula outcomes. Am J Nephrol 2016;44(6):426–7. https://doi.org/10.1159/000452429.
[32] Hammes M, McGill RL, Basu A, Blicharski T, Delaney K. Hemodynamic effects of hemodialyzer pump speed on arteriovenous fistulas, Clin Nephrol 2019;91 (2019) - March (138 - 146)(0301-0430 (Print)). 10.5414/CN109456.
[33] Irfan H, Ooi GS, Kyin MM, Ho P. Revealing maximal diameter of upper limb superficial vein with an elevated environmental temperature. Int J Chronic Dis 2016;2016:8096473. https://doi.org/10.1155/2016/8096473.
[34] Schneider CA, Rasband WS, Eliceiri KW. NIH Image to ImageJ: 25 years of Image Analysis HHS Public Access. 2012.
[35] Vitello DJ, Ripper RM, Fettiplace MR, Weinberg GL, Vitello JM. Blood density is nearly equal to water density: A validation study of the gravimetric method of measuring intraoperative blood loss. J Vet Med 2015;2015:. https://doi.org/10.1155/2015/152730152730.
[36] Nader E, Skinner S, Romana M, Fort R, Lemonne N, Guillot N, et al. Blood rheology: key parameters, impact on blood flow, role in sickle cell disease and effects of exercise. Front Physiol 2019;10.
[37] Albayrak R, Yuksel S, Colbay M, Degirmenci B, Acarturk G, Haktanir A, et al. Hemodynamic changes in the cephalic vein of patients with hemodialysis arteriovenous fistula. J Clin Ultrasound 2007;35(3):133–7. https://doi.org/10.1002/jcu.20307.
[38] Bolelli F, Allegretti S, Baraldi L, Grana C. Spaghetti labeling: directed acyclic graphs for block-based connected components labeling. IEEE Trans Image Process 2020;29(1):1999–2012. https://doi.org/10.1109/TIP.2019.2946979.
[39] Bradski G. The OpenCV Library. Dr Dobb's Journal of Software Tools 2000. PubMed PMID: opencv_library.
[40] Baskurt OK, Meiselman HJ. Blood Rheology and Hemodynamics. Semin Thromb Hemost 2003;29(05):435–50. https://doi.org/10.1055/s-2003-44551.
[41] Boghosian ME, Hammes MS, Cassel KW, Akherat SMJ, Coe F. Restoration of wall shear stress in the cephalic vein during extreme hemodynamics. J Med Eng Technol 2018;42(8):617–27. https://doi.org/10.1080/03091902.2019.1591534.
[42] Van Tricht I, De Wachter D, Tordoir J, Verdonck P. Hemodynamics and complications encountered with arteriovenous fistulas and grafts as vascular access for hemodialysis: A review. Ann Biomed Eng 2005;33(9):1142–57. https://doi.org/10.1007/s10439-005-5367-X.
[43] Colley E, Carroll J, Anne S, Shannon T, Ramon V, Tracie B. A longitudinal study of the arterio-venous fistula maturation of a single patient over 15 weeks. Biomech Model Mechanobiol 2022;21(4):1217–32. https://doi.org/10.1007/s10237-022-01586-1.
[44] Dhar P, Eadon M, Hallak P, Munoz RA, Hammes M. Whole blood viscosity: Effect of hemodialysis treatment and implications for access patency and vascular disease. Clin Hemorheol Microcirc 2012;51:265–75. https://doi.org/10.3233/CH-2012-1532.
[45] Shirazian S, Rios-Rojas L, Drakakis J, Dikkala S, Dutka P, Duey M, et al. The effect of hemodialysis ultrafiltration on changes in whole blood viscosity. Hemodial Int 2012;16(3):342–50. https://doi.org/10.1111/j.1542-4758.2012.00671.x.
[46] Jain A, van der Meer AD, Papa AL, Barrile R, Lai A, Schlechter BL, et al. Assessment of whole blood thrombosis in a microfluidic device lined by fixed human endothelium. Biomed Microdevices 2016;18(4). https://doi.org/10.1007/s10544-016-0095-6.
[47] Rios DRA, Carvalho MG, Figueiredo RC, Ferreira CN, Rodrigues VL, Souza RA, et al. ADAMTS13 and von Willebrand factor in patients undergoing hemodialysis. J Thromb Thrombolysis 2012;34(1):73–8. https://doi.org/10.1007/s11239-012-0682-1.
[48] Zawaski S, Hammes M, Balasubramanian V. Alternatively Spliced Human Tissue Factor and Thrombotic Tendencies in Hemodialysis Patients. 2010.
[49] Péquériaux NC, Fijnheer R, Gemen EF, Barendrecht AD, Dekker FW, Krediet RT, et al. Plasma concentration of von Willebrand factor predicts mortality in patients on chronic renal replacement therapy. Nephrol Dial Transplant 2012;27(6):2452–7. https://doi.org/10.1093/ndt/gfr735.